



# High-Speed Imaging of the Ultrasonic Deagglomeration of Carbon Nanotubes in Water

ZHUOCHENG XU,<sup>1</sup> CATHERINE TONRY ,<sup>2</sup> CHRISTOPHER BECKWITH ,<sup>2</sup>  
ANDREW KAO ,<sup>2</sup> HAYLEY WONG,<sup>1</sup> MILO S.P. SHAFFER ,<sup>3,4</sup>  
KOULIS PERICLEOUS ,<sup>2</sup> and QIANQIAN LI ,<sup>1,5</sup>

1.—Department of Aeronautics, Faculty of Engineering, Imperial College London, London, UK. 2.—School of Computing and Mathematical Sciences, Faculty of Engineering and Science, University of Greenwich, London, UK. 3.—Department of Chemistry, Faculty of Natural Sciences, Imperial College London, London, UK. 4.—Department of Materials Science, Faculty of Engineering, Imperial College London, London, UK. 5.—e-mail: qianqian.li@imperial.ac.uk

Ultrasonic treatment is effective in deagglomerating and dispersing nanoparticles in various liquids. However, the exact deagglomeration mechanisms vary for different nanoparticle clusters, owing to different particle geometries and inter-particle adhesion forces. Here, the deagglomeration mechanisms and the influence of sonotrode amplitude during ultrasonication of multiwall carbon nanotubes in de-ionized water were studied by a combination of high-speed imaging and numerical modeling. Particle image velocimetry was applied to images with a higher field of view to calculate the average streaming speeds distribution. These data allowed direct comparison with modeling results. For images captured at higher frame rates and magnification, different patterns of deagglomeration were identified and categorized based on different stages of cavitation zone development and for regions inside or outside the cavitation zone. The results obtained and discussed in this paper can also be relevant to a wide range of carbonaceous and other high aspect ratio nanomaterials.

## INTRODUCTION

Over the last few decades, real-life applications of nanoparticle-containing materials have been investigated. These materials have been selected as potential candidates in areas ranging from electrical devices<sup>1</sup> to structural composites.<sup>2</sup> However, due to their high surface area and energy, nanoparticles tend to form agglomerates in their as-received state or during processing.<sup>3</sup> High-frequency vibration treatment, e.g., ultrasound treatment (UST) is a proven method for deagglomerating nanoparticles in various liquids,<sup>4</sup> primarily through acoustic cavitation and streaming. Once the acoustic pressure reaches a certain threshold (the Blake threshold<sup>5</sup>), bubbles will be generated in the liquid

medium. These bubbles can grow and collapse violently<sup>6</sup> within one or several acoustic cycles.<sup>7</sup> The bubble implosion results in dramatic local conditions with emitted shockwaves, pressure of  $O(10^4 \text{ atm})$  and temperature of  $O(10^4 \text{ K})$ .<sup>8</sup> These conditions are sufficient to overcome the Van der Waal's attraction among the individual nanoparticles, initiating deagglomeration, and may even break covalent bonds between fused primary particles, or break the primary particles themselves, particularly if they have high aspect ratio.<sup>9</sup> In contrast to this localized acoustic cavitation effect, UST also leads to macroscopic acoustic streaming, which further disperses the separated particles in the bulk liquid.<sup>10</sup> In addition to these two primary effects, many researchers also propose that cavitation bubbles improve surface wetting, leading to a sono-capillary effect, which promotes the penetration of liquid into cracks and interstitial spaces

inside agglomerates.<sup>6,11</sup> These events effectively disperse the nanoparticles by promoting implosion of cavitation bubbles inside the agglomerate.<sup>6</sup>

Carbon nanotubes (CNTs) are one of the most widely studied nano-systems, for their excellent intrinsic properties and wide range of applications. They are particularly challenging to disperse due to their low chemical reactivity, poor compatibility with solvents, and strong inter-nanotube attractions. Their high aspect ratio adds further complexity as they form bundles or entangled aggregates of strong particles. UST is most commonly accomplished in water, often with a small-molecule surfactant, such as sodium dodecyl sulfate (SDS), sodium dodecylbenzene sulfonate (SDBS), sodium cholate, or a macromolecular amphiphile such as DNA, poly(vinyl alcohol) (PVA), or proteins.<sup>12</sup> The dispersion step is a critical step towards separations, devices fabrication, fundamental scientific studies of single particle properties, or the preparation of nanocomposite/hybrid systems. The exact dispersion mechanisms that occur during UST depend on the dimensions and physical properties of the nanoparticles. A further complexity in the case of CNTs is that scission may occur, attributed to axial acceleration or buckling of these high aspect ratio particles.<sup>9,13</sup> According to Huang et al.<sup>9,13</sup>, the implosion of cavitating bubbles near CNTs not only leads to individual nanotube separation but also shortening above a critical shear-lag length. They attributed this scission mechanism to the stress built up along CNTs by the radial acceleration during the implosion of nearby bubbles. In contrast, Guido et al.<sup>14</sup> simulated the dynamic behavior of a single CNT near a collapsing bubble as a function of length. This model assumes that the CNT aligns tangentially to the growing bubble during the initial stages; the results suggest a length-dependent bending or rotation which may break the CNT by buckling or stretching above a critical threshold.

Although the mechanisms behind multiwall carbon nanotube (MWCNT) deagglomeration are discussed conceptually in the literature, validation based on in-situ experimental analysis is limited. Other than simple visual observations, evidence for nanoscale CNT deagglomeration during UST is usually only qualitatively supported by post-mortem observations under optical transmission microscopy<sup>15</sup> or electron microscopy.<sup>16</sup> Alternatively, averaged information about dispersion concentration and quality can be obtained by dynamic light scattering and ultraviolet-visible spectroscopy.<sup>17</sup> However, none of these techniques provides information related to the spatial distributions of the CNTs in the bulk liquid. Systematic studies of the influence of UST parameters on the dispersion state of CNTs are limited, with most of the literature focusing only on duration of UST (related to the total power input).<sup>13,16–18</sup> In 2019, Zaib and Ahmad used a response surface methodology (RSM) to design a set of experiments for parametric studies

during UST.<sup>19</sup> In their work, UST amplitude, sonication time, and pulse on and off time were varied during UST of MWCNTs in water suspension. Based on the experimental results, a semiempirical expression was developed to relate the relationships between the various UST parameters, resulting average diameters, and size distributions of MWCNT aggregations. By analyzing the surface plot generated by their semiempirical model, the amplitude of probe vibration was found to have the greatest impact on both dispersion parameters. After scanning the entire range of the four UST parameters, optimized parameters for their particular configuration were found to be 89 s (UST duration), 144  $\mu\text{m}$  (amplitude) and 44/30 s (total pulse on/off time).

Due to advances in high-speed imaging, readily accessible high-speed cameras are now capable of reaching frame rates close to a few thousand frames per second,<sup>20</sup> which is close to the frequency of UST generators. Therefore, the dynamic behavior of bubbles and their interactions with agglomerates during UST can be captured and analyzed. Morton et al.<sup>20</sup> used high-speed imaging to study the sonoxfoliation of graphite, similar to the deagglomeration process, in deionized (DI) water. By adjusting the distance between graphite and sonotrode, two mechanisms that potentially lead to graphite layer exfoliation were identified. With the graphite within the developed cavitation zone (CZ), powerful shockwaves were capable of initiating graphite exfoliation. When the graphite was placed outside the CZ, interlayers of graphite were first expanded by the translational force produced by the oscillation of the interlayer bubbles, then subsequently exfoliated by shockwaves and micro-jets produced during the implosion of the nearby micro-bubbles. The first-ever high-speed observation of UST induced deagglomeration of nanoparticles was discussed by Eskin et al. in 2019,<sup>21</sup> by comparing the images of MgO agglomerates before and after surface bubble implosion. They considered that the deagglomeration process initiated from surface rather than internal bubble clusters, proceeding by chipping off individual particles from the surface rather than rupturing of the agglomerate from within. Recently, Abhinav et al.<sup>22</sup> reported a more detailed in-situ study of the deagglomeration process of MgO and SiO<sub>2</sub> particles in water. Based on the images captured during UST, they proposed two deagglomeration mechanisms, which resemble the findings of Morton et al.<sup>20</sup> Specifically, they identified the instantaneous fragmentation of clusters by a high-intensity bubble cloud in the CZ, erosion of agglomerates caused by oscillation of bubbles on the surface, and agglomerate rupture due to the coalescence and implosion of micro-bubbles. In addition, they reported a new mechanism whereby the oscillation of micro-bubbles in the liquid tends to follow small floating agglomerates, further promoting deagglomeration after bubble implosion.

Computational models have been developed to investigate these phenomena. On the acoustic side, nonlinear Helmholtz models have been previously used to address such problems.<sup>23</sup> Previous work at the University of Greenwich<sup>24</sup> has demonstrated the use of the nonlinear Helmholtz model to simulate streaming from a sonotrode in a direct-chill casting launder. Attenuation caused by the change in speed of sound due to the presence of bubbles has also been taken into account when predicting fluid flow from acoustic streaming.<sup>25</sup>

In this paper, the dispersion of MWCNTs in DI water during UST was captured for the first time by using high-speed imaging. The amplitude of the UST generator was varied to study the influence of input UST intensity. Furthermore, the distributions of average streaming flow speed at different amplitudes were calculated and compared with simulations for model validation and theoretical studies. Different MWCNT deagglomeration mechanisms were also identified and categorized based on different stages of cavitation zone development and for regions inside or outside the cavitation zone.

## EXPERIMENTAL AND METHODOLOGY

### Preparation of Nanofluid

In each test, 27 mg of NC-7000 MWCNTs (provided by NANOCYL with an average diameter of 9.5 nm and length of 1.5  $\mu\text{m}$ ) and 54 ml of DI water were mixed in a transparent rectangular vessel (3B scientific) with an inner dimension of  $77 \times 74 \times 23 \text{ mm}^3$  (length  $\times$  height  $\times$  thickness) to obtain a concentration of 500 mg/l. This concentration was determined by the trial tests to avoid the mixture becoming opaque immediately after starting the UST generator, but is also typical of concentrations used in CNT dispersion studies. After initial mixing, the mixture was gently shaken and settled for 5 min to distribute the MWCNT agglomerates in DI water and allow some of them to sink to the bottom of the vessel.

### UST System and Parametric Study

The ultrasonic system used in this study was the Sonic VCX 750 processor equipped with a standard 12.7-mm-diameter and 139.0-mm-long Ti64 probe. The UST generator had a fixed frequency of 20 kHz with adjustable amplitude. In this study, the tested oscillation amplitudes of the sonotrode were 24  $\mu\text{m}$ , 36  $\mu\text{m}$ , and 48  $\mu\text{m}$ , equivalent to 20%, 30% and 40% of the full power, respectively; while other parameters such as the probe immersion depth and testing temperature were fixed at 10 mm and 20°C.

### High-Speed Imaging Setup

For the imaging system, a high-intensity LED was used as a light source. A Phantom VEO 640 high-speed camera and Tokina 100 mm F2.8 macro lens were used for high-speed filming. The camera

was controlled by the Phantom camera control software installed on a PC that enabled camera parameters such as resolution, frame rate, and exposure to be adjusted. In this study, two resolutions ( $2560 \times 1600$  and  $640 \times 480$ ) were used to capture the distribution of MWCNTs in the bulk solution [using high-resolution for a wider field of view (FoV)] and the dynamic interaction between cavitation bubbles and agglomerates (using lower resolution for a higher frame rate) in each amplitude. The regions of interest (ROI) and detailed parameters for each resolution are indicated in Fig. 1a. Due to the limited RAM in the camera, the recording time for both resolutions was around 10 s. Figure 1b and c are snapshot examples for these two different resolutions.

### Data Analysis for High-Speed Imaging

Images captured at wider FoV were used to analyze the fluid motion within the vessel. For each test, 700 images captured between 7.0 s and 7.5 s after starting the UST were selected for particle image velocimetry (PIV) processing. This time period of 7.0–7.5 s was chosen as the nanoparticles were then relatively evenly distributed (Fig. 1b). LaVision Davis 10 with Flowmaster package was used for image processing and PIV analysis. The images were first rescaled according to their pixel size. Then, three geometric masks were used to cover the positions of the sonotrode tip, floating particles, and the bottom wall of the vessel to remove their influence during PIV analysis. A subtract time filter with a Gaussian average and a subtract sliding background filter were then used to eliminate the influence of background noise. The filtered images were processed by the time-resolved 2D-PIV method in Davis. The PIV results were obtained after 4 iterations with varied interrogation window size and overlapping from  $64 \times 64$  pixels and 50% overlap in the first pass to  $16 \times 16$  pixels (spatial resolution: 0.48 mm) and 75% overlapping in the final pass.

The films captured at the higher frame rate were used to study the deagglomeration mechanisms of MWCNTs. For each film, all of the deagglomeration events that could be identified by eye within the first 4 s of US were identified and summarized. Then, these deagglomeration events were compared and categorized based on their times, locations, and features.

### Numerical Modeling

A three-dimensional coupled numerical model has been developed using COMSOL Multiphysics to predict the acoustic streaming within the vessel. The vessel dimensions and process conditions in the numerical model were assumed to be the same as the experimental work. The Navier-Stokes equations coupled with a nonlinear Helmholtz-type model<sup>26</sup> were used to simulate the acoustic pressure

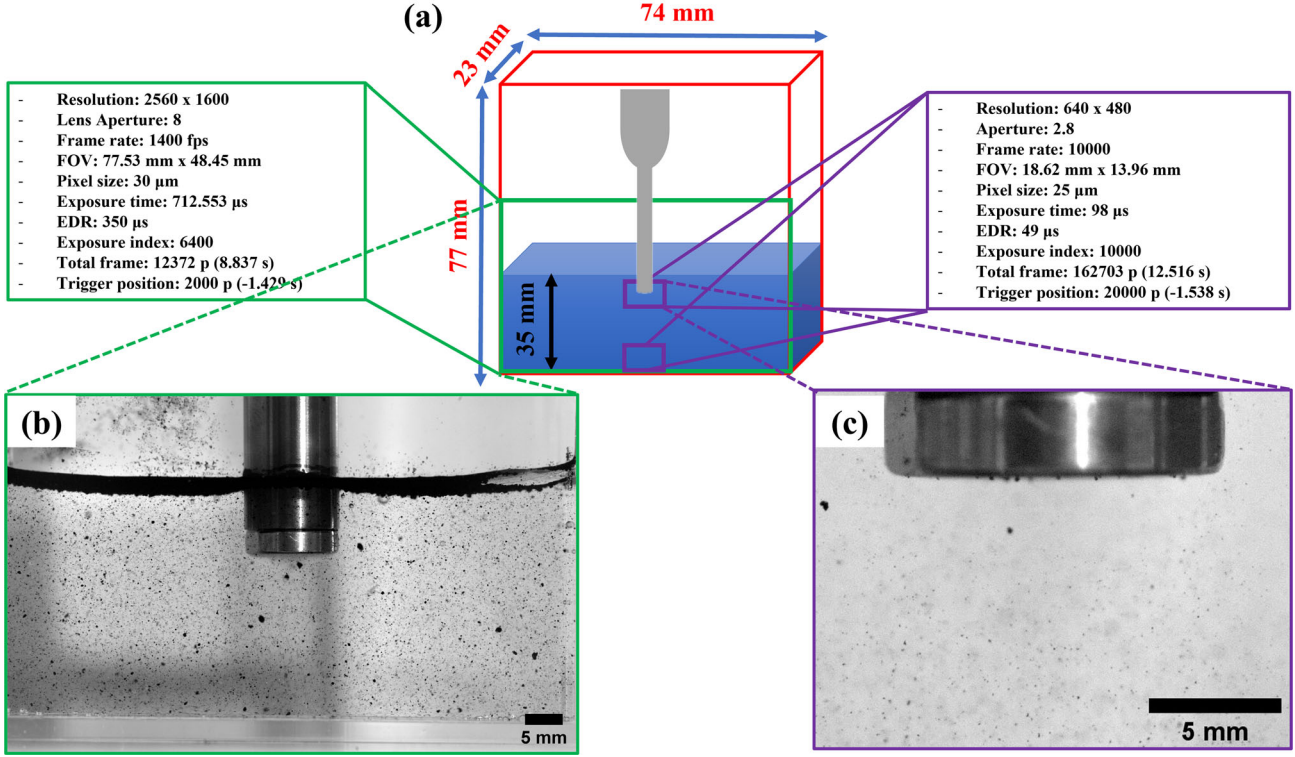


Fig. 1. (a) A sketch of ROI captured during high-speed imaging in each test. The camera setting for each ROI is summarized in the text box next to the sketch. Snapshots after 7 s of UST given with resolutions of (b)  $2560 \times 1600$  and (c)  $640 \times 480$ .

field and acoustic streaming, including the effect of cavitation, as follows:

$$\nabla^2 P + k_m^2 P = 0, \quad (1)$$

where  $P$  represents the complex acoustic pressure field and  $k_m^2$  is the modified wave number

$$k_m^2 = \left(\frac{\omega}{c}\right)^2 - \left(\frac{\mathcal{A}(P)}{|P|} + i \frac{\mathcal{B}(P)}{|P|}\right) \quad (2)$$

where  $\omega$  is the angular frequency and  $c$  the speed of sound in the liquid. and  $\mathcal{B}$  are the dissipation functions as defined by Trujillo<sup>27</sup> given by

$$\mathcal{A} = -\frac{\rho_l \omega^2}{\pi} \int_0^{2\pi} \frac{\partial \beta}{\partial t} \sin t dt, \mathcal{B} = -\frac{\rho_l \omega^2}{\pi} \int_0^{2\pi} \frac{\partial \beta}{\partial t} \cos t dt \quad (3)$$

where  $\rho_l$  is the liquid density,  $t$  is time and  $\beta$  is the void fraction defined by

$$\beta = \frac{4}{3} \pi R^3 N \quad (4)$$

where  $R$  is the bubble radius and  $N$  the number of bubbles. The bubble radii were obtained using a coupled a cavitation model using the Keller-Miksis (KM) approach<sup>28</sup>

$$\begin{aligned} & \left(1 - \frac{\dot{R}}{c}\right) R \ddot{R} + \frac{3}{2} \dot{R}^2 \left(1 - \frac{\dot{R}}{3c}\right) \\ & = \frac{1}{\rho_l} \left(1 + \frac{\dot{R}}{c} + \frac{R}{c} \frac{d}{dt}\right) [p_l - p(t)], \end{aligned} \quad (5)$$

where  $p_l$  represents the pressure at the liquid gas interface. The pressure  $p(t) = p_0(1 - A \sin(\omega t))$  accounts for both the atmospheric and acoustic pressures. For the parameter  $\mathcal{A}$ , individual bubble simulations were performed for a range of pressures following previous work.<sup>24</sup> These computer coefficients were referred to as a function of the local pressure in the Helmholtz equation. For the acoustic model “sound hard” ( $\nabla P \cdot \hat{n} = 0$ ) boundaries were used at all sides and the water free surface had a “sound soft” boundary ( $P = 0$ ). For the sonotrode, the pressure gradient at the boundary was calculated from the acceleration of the sonotrode ( $\frac{dP}{dy} = \frac{\rho_l \omega^2 h}{2}$ ) where  $h$  is the peak-to-peak amplitude.

To model the acoustic streaming, the results from the acoustic cavitation model were one-way coupled to a steady-state turbulent flow model in COMSOL Multiphysics, using the conservation and momentum equations

$$\rho_l \nabla \cdot v = 0 \quad (6)$$

$$\rho_l(v \cdot \nabla)v = \nabla \cdot \left[ -p_f + (\mu + \mu_T)(\nabla v + (\nabla v)^T) \right] + F_s \quad (7)$$

where  $v$  is the fluid velocity,  $p_f$  is the fluid pressure,  $\mu$  is the dynamic viscosity,  $\mu_T$  the turbulent viscosity calculated using the k- $\epsilon$  model, and  $F_s$  the acoustic streaming force,

$$F_s = \nabla(\rho_l v_a \otimes v_a) \quad (8)$$

where  $v_a$  is the acoustic velocity ( $v_a = \frac{\nabla P}{\rho_l \omega}$ ). The domain is based on the experimental vessel, measurements  $77.18 \times 74.16 \times 23.75 \text{ mm}^3$  with a water depth of 29.46 mm. Material properties used in the model are shown in Table I. Boundary conditions for the flow model were no-slip (with wall functions for the turbulence model) on all surfaces except the water air interface where a slip condition was used.

## RESULTS AND DISCUSSION

### Images and Microstructure

Before UST, most of the MWCNT clusters were floating at the top of the liquid, even 5 min after the vessel was shaken and settled after adding the MWCNTs, probably owing to their low density and highly porous structure. After 10 s of UST, most of the floating MWCNTs were observed to be dragged and evenly dispersed into the water underneath. Figure 2 shows a significant change in MWCNT morphology before and after 10 s of UST. In the as-received state (Fig. 2a), the densely packed agglomerates of MWCNTs were approximately globular with a random size distribution in the range 10–100  $\mu\text{m}$ . Examining the image at higher magnification (Fig. 2b) taken from the inside of one agglomerate, the individual CNTs can be seen wound tightly together forming an entangled network. In comparison, after 10 s of UST, the CNTs presented much smaller agglomerates with individual sizes around a few micrometers (Fig. 2c and Supplementary Fig. S1). At higher magnification in Fig. 2d, the network structure can still be observed; but different from Fig. 2b, many individual tubes can also be observed either lying separated from the agglomerates, or only loosely connected.

### Simulated Acoustic Pressure Distribution

The numerical modeling predicted the acoustic pressures and streaming velocities for the different

sonotrode amplitudes given in Fig. 3. The results show that increasing sonotrode vibration amplitude increases the maximum pressures from 389 kPa to 566 kPa; however, the overall distribution of acoustic pressure does not change significantly in regions far from the sonotrode and so only an example case for 48  $\mu\text{m}$ . Figure 3 also plots the Blake threshold for the 48  $\mu\text{m}$  sonotrode amplitude. This shows the active cavitation region below the black line in the slice, and under the isosurface in Fig. 3b. This demonstrates that there is a significant region of cavitation.

### Average Velocity Distribution

The deagglomeration and dispersion of MWCNTs were successfully captured by the high-speed camera. Using PIV, the experimental images were converted to give the averaged fluid velocity due to acoustic streaming for differing sonotrode amplitudes (Fig. 4a–c) along with the corresponding standard deviation (Fig. 4d–f). The PIV procedure was not able to capture the main downward flow jet, directly below the sonotrode, due to the excessive velocities. This region appears blank in Fig. 4a–c and coincides with the highest standard deviations from the PIV measurements. The numerical modeling results predict that there should be a high-velocity jet below the sonotrode, as observed qualitatively in the experiment (Supplementary video 1). These results can be plotted as a slice of the numerical solution in the mid-plane of the vessel, containing the center of the sonotrode (Fig. 4g–i), or as averaged velocities along the  $z$  direction representing a ‘projection’ of the velocity field (Fig. 4j–l). A direct comparison of the numerical and experimental data is difficult as PIV is a 2-dimensional representation of what is inherently a 3-dimensional particle velocity field, due to the relatively large length scale in  $z$  and uncertain focal depth (the focusing plane for this study was chosen as the middle cross-section of the sonotrode).

The simulation highlights the 3-dimensional nature of the flow (Fig. 5), showing relatively high velocities on the front and rear walls of the vessel. The high-speed jet introduces several problems for PIV measurements in the region below the sonotrode. The numerical model predicts flow velocities in the order of 1 m/s and with the high-speed camera capturing 1400 fps, particles in this region may move almost 1 mm between successive frames, which is almost twice the PIV spatial resolution (0.48 mm). The high flow velocities on the front and back walls are in the positive  $y$  direction and so particles circulating on this return path will be traveling in the opposite direction to those directly under the sonotrode. From an observation perspective, particles will be traveling in both directions and hence it becomes increasingly difficult to track individual particles, hence the large standard deviations in this region.

**Table I. Material properties in numerical modeling**

Parameter	Water
Sound speed (m/s)	1482
Density ( $\text{kg/m}^3$ )	998
Surface tension (N/m)	0.072
viscosity (mPa s)	1.00

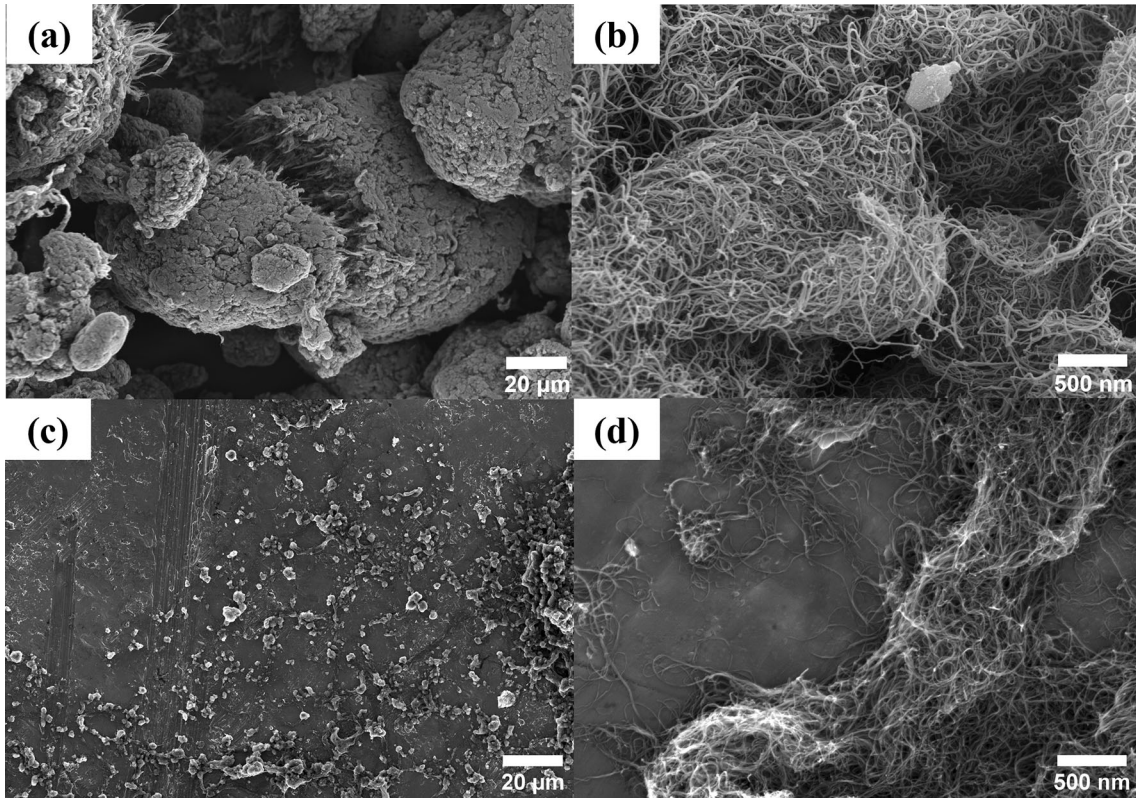


Fig. 2. SEM images of as-received MWCNT agglomerates (a) at low magnification and (b) at higher magnification. SEM images of CNT agglomerates after 10 s of UST at 40% amplitude (c) at low magnification and (d) at higher magnification.

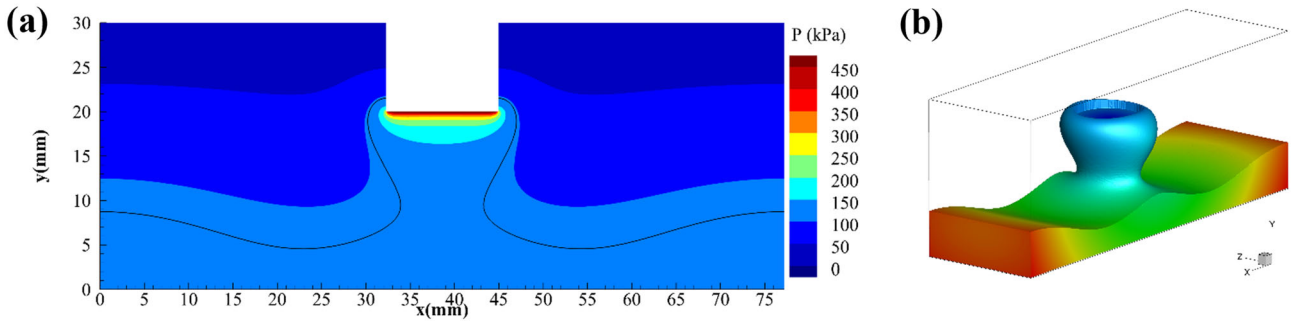


Fig. 3. Acoustic pressure for sonotrode amplitudes of 48  $\mu\text{m}$ . (a) 2D slice of pressure distribution at halfway vessel thickness, black line represents the Blake threshold. The origin for this 2D plot was selected as the left bottom corner in the central section of the vessel. (b) An isosurface of the Blake threshold. The cartesian coordinate is indicated in the inset in (b).

Nevertheless, despite these complications, away from the sonotrode, in regions of bulk flow with slower velocities ( $|U| < 0.4 \text{ m/s}$ ) and low standard deviation in the PIV results, there is a clear qualitative resemblance between the experimental and simulated data at the 3 different amplitudes [comparing Fig. 4(a–c) with (g–i), respectively]. These flow speeds and patterns are also consistent with previous PIV measurement where similar probe amplitudes were used.<sup>10,23,29</sup> The numerical model predicts the relative size of the stagnation point at the lower wall. There is also an excellent agreement between the number and size of fluid

vortices. The  $xy$  slice plots also show  $xy$  streamlines, demonstrating the vortices and direction of flow.

### Observed CNT Deagglomeration Mechanisms

From the images captured at the higher frame rate, different types of MWCNT deagglomeration mechanisms were found. In the following paragraphs, these mechanisms are discussed based on their timing relative to a stable CZ development (before and after) and relative proximity to the CZ (direct and indirect interaction). It is worth mentioning that all these mechanisms have been observed at all three amplitudes tested in this work,

# High-Speed Imaging of the Ultrasonic Deagglomeration of Carbon Nanotubes in Water

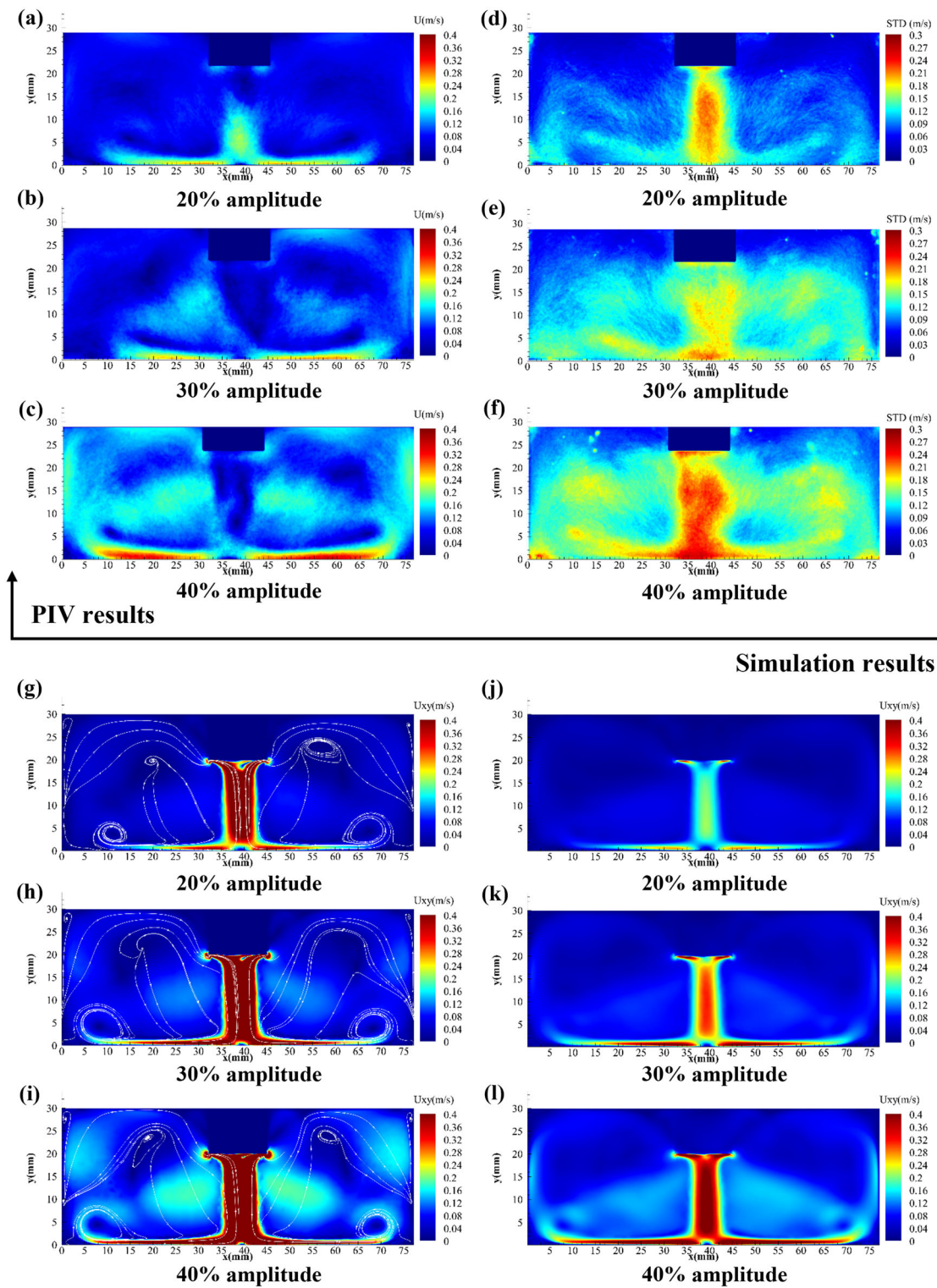


Fig. 4. Plots of velocity magnitude for the average over 0.5 s for experimental PIV data (a–c), and standard deviation of the PIV data (d–f), a center  $xy$  slice in the numerical model (g–i), the average velocity in  $z$  for the numerical model (j–l); note, numerical and experimental scale bars have been matched to highlight the bulk flow. The coordinate axis system is the same as in Fig. 3.

but the examples shown represent the most dominant cases.

*During the Development of the CZ*

The deagglomeration process initiated immediately after the UST was activated. For the top ROI,

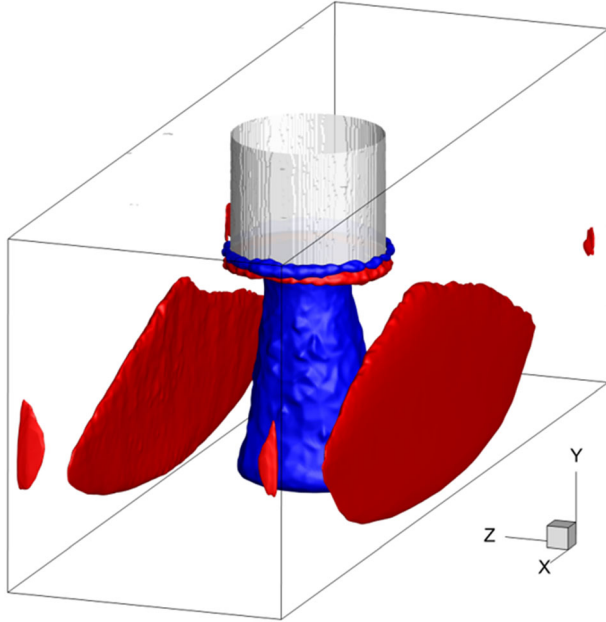


Fig. 5. Isosurface of velocities [-0.2 (blue), 0.2 (red) m/s] in the y direction from the simulation for the 40% magnitude.

a transient bubble cloud, which was generated and annihilated within one sonotrode oscillation cycle, was found to appear, grow and stabilize within 18.8 ms (Fig. 6b–e). As shown in Fig. 6e, the stabilized CZ acquired a typical conical shape directly under the sonotrode, which was similar to previous observations.<sup>30</sup> Besides this transient bubble cloud, some bubbles within the CZ may coalesce and leave the CZ in the form of micro-bubble clusters, by following the downward streaming flow (Fig. 6f). Figure 6b–e show the breaking of agglomerates during the development of the CZ. Immediately after the UST generator was activated, the agglomerates attached to the sonotrode probe firstly coalesced with their neighbors and subsequently ruptured during the emergence of the bubble cloud from the tip surface. During the rupturing of these agglomerates, small debris fragments and a ‘mist’ were formed which were believed to be the smaller MWCNT clusters and individual tubes broken from the agglomerate surface. By considering the extensive implosion of bubbles in the CZ, the breaking of MWCNT agglomerates can be explained by the shockwave generated during implosion, as described in other systems.<sup>20,31</sup>

For the bottom ROI, a bubble appeared and grew from the surface of an agglomerate located in the center of the bottom wall, immediately following UST activation (Fig. 7a–c). In the next few milliseconds, this bubble migrated into the center of the agglomerate and formed a micro-bubble cluster, probably by coalescence with other surface bubbles or existing air pockets inside the agglomerate. As

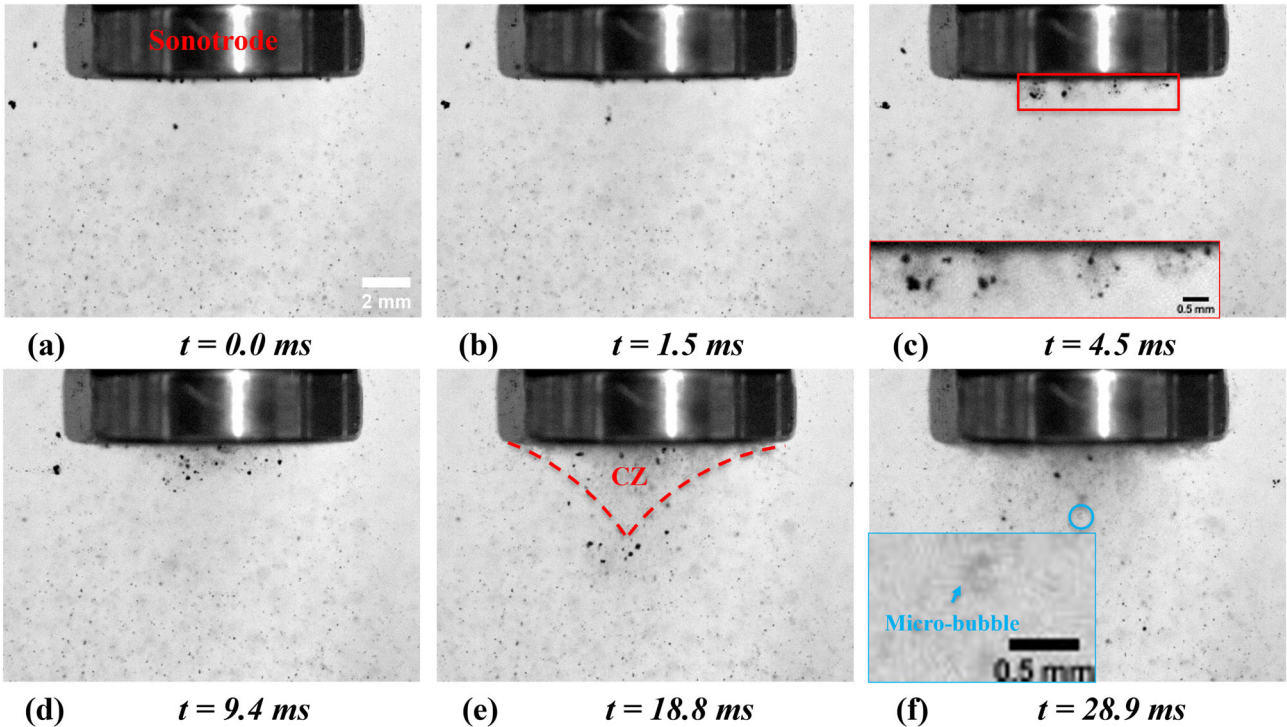


Fig. 6. Images captured at the top ROI at the beginning of UST with a 40% probe amplitude. The insets in (c) and (f) are higher magnifications of the labeled features. The elapsed time after the sonotrode was switched on is given at the bottom of each picture (See supplementary video 2).

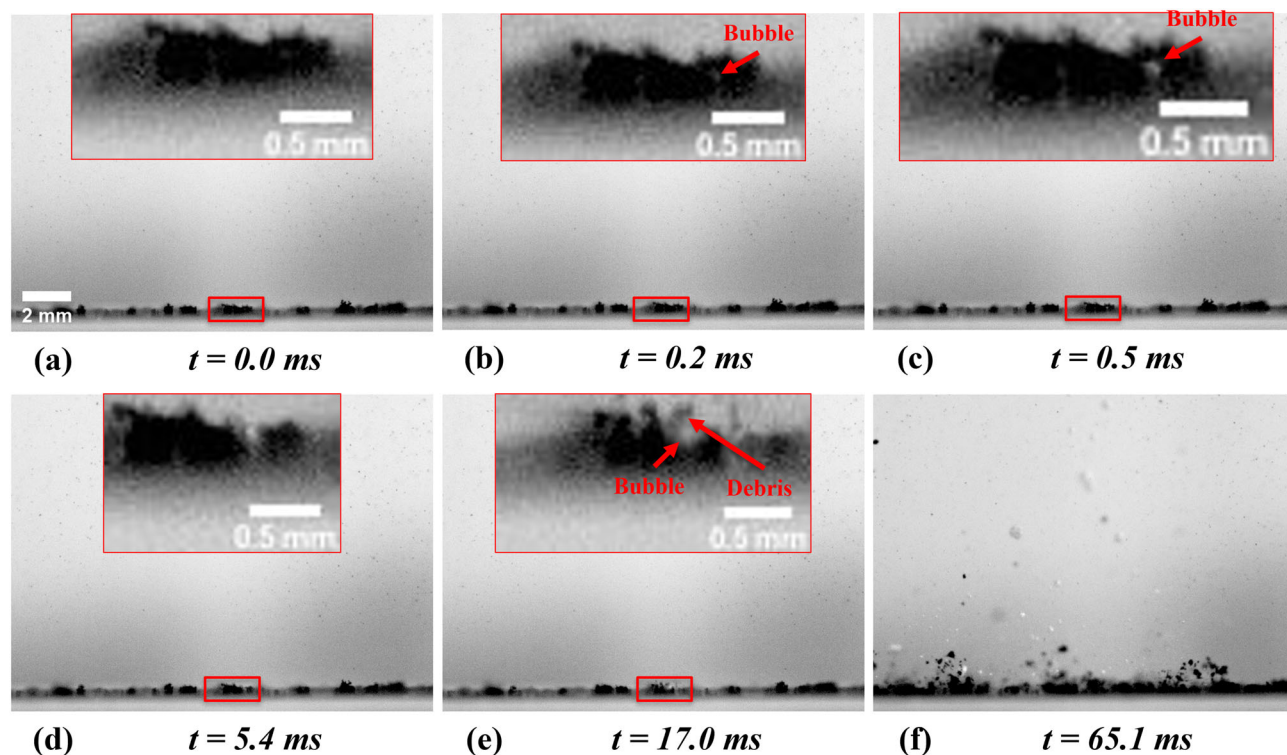


Fig. 7. Images captured at the bottom ROI with a 40% probe amplitude at the beginning of UST. The insets are higher magnifications of the labeled features. The elapsed time after the sonotrode was switched on is given at the bottom of each picture (See supplementary video 3).

the CZ developed further (Fig. 6), this micro-bubble cluster repeatedly collapsed and rebounded within the agglomerate, peeling off small fragments from its surface. This erosion phenomenon was similar to Priyadarshi et al.<sup>22</sup> observation. In their report, the generation of the surface bubble was attributed to acoustic waves from the sonotrode while the particle breaking was believed to be due to the combined effect of shockwaves and microjets generated during the implosion of the micro-bubbles. After the jet flow reached the bottom of the vessel, this agglomerate was dispersed by the recirculating flow formed at the bottom wall (Fig. 7f).

#### *Deagglomeration Due to Direct Interaction with the Stabilized CZ*

In contrast to the obvious breaking events during the development of CZ (Fig. 6), many of the particles showed no obvious change after they passed through the stabilized CZ (Fig. 8a) 20% amplitude and (Fig. 8b) 40% amplitude. However, some particle deagglomeration is expected whenever the agglomerates pass through the CZ, due to the pressure force generated by the imploding cavitation bubbles (measured as a few MPa in previous work with a similar amplitude<sup>20,22</sup>), which is higher than the Van der Waals attraction (around 16 kPa based on Huang's model<sup>9</sup>) that holds the MWCNT

agglomerates together. The 'mist' formation observed once the bubbles imploded next to the agglomeration (see supplementary video 4-1) can plausibly be attributed to the breaking off of small particles from the surface of the agglomerate. Unfortunately, the camera could not resolve individual fragments due to its limited resolution (30  $\mu\text{m}$ ). It is also possible that the agglomerates became loosened and separated after being brought back to the CZ by circulated flow for few times. However, the duration of our imaging was relatively short (around 10 s). If a particle is moving at an average speed of 0.3 m/s (estimated based on Fig. 4.), it will only pass through the ROI around 20 times during the filming period (if we assume this particle follows the near rectangular motion in one side of the vessel). Besides, it is extremely difficult to identify a specific agglomerate whenever it is passing through the ROI.

On the other hand, two representative deagglomeration events were observed inside the CZ, including peeling Fig. 8c and rupture Fig. 8d. In the former, multiple layers of fragments peeled off (at 909.7 ms) following the implosion of cavitation bubbles (at 909.2 ms) near the agglomerate. This phenomenon is similar to the 'flipping page' mechanism reported during the sono-exfoliation of graphite.<sup>20</sup> By considering the similarity of these two carbonaceous substances, the observed 'peeling-off'

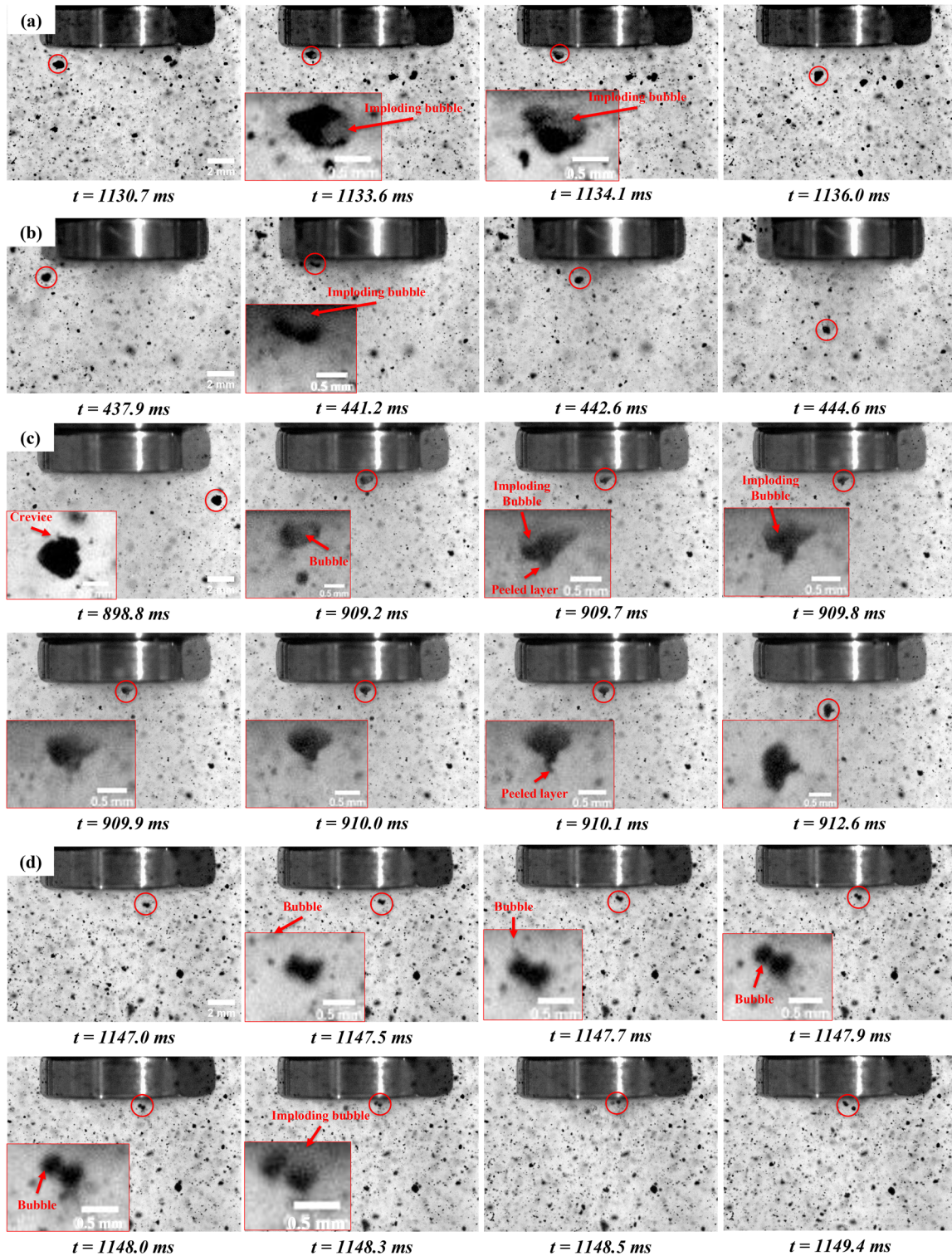


Fig. 8. Snapshots of agglomerates interacting directly with CZ in the stabilized CZ stage. Particles show no obvious breaking after entering the CZ at 20% (a) (See supplementary video 4-1) and 40% (b) of amplitude (See supplementary video 4-2). (c) A particle peeling off from the surface of an agglomerate within the CZ (30% of amplitude) (See supplementary video 5). (d) Particle rupture after entering the CZ (20% of amplitude) (See supplementary video 6). The elapsed time after the sonotrode was switched on is given at the bottom of each picture.

mechanism can be explained by layers of non-intertwined MWCNT clusters broken from the surface of their parent agglomerate due to the shockwave generated during the bubble implosion.

Rupture is illustrated by the image sequence in Fig. 8d, where an agglomerate was broken in half at 1148.5 ms. Before breaking, this agglomerate interacted significantly with a bubble in the CZ (1147.7

ms), changing its shape from nearly rectangular to 'pear'-like at 1147.9 ms. By zooming into this frame, a bubble was identified in the neck of the 'pear' and it subsequently split the two sides apart. One possible explanation for this phenomenon is the coalescence between the bubble from the CZ and the tiny bubble on the surface, or an air pocket inside the agglomerate.<sup>20–22</sup> At 1148.3 ms, the two parts disintegrated simultaneously with the implosion of the bubble located at the center and the surrounding bubble cloud.

#### *Deagglomeration Due to Indirect Interaction with the Stabilized CZ*

Considering the hydrophilic nature of the CNTs<sup>32</sup> and porous structure in their agglomerates, as in Fig. 2, bubbles or air pockets were expected on the surface and inside the MWCNT agglomerates after adding them to water. These pre-existing bubbles were subjected to continuous oscillation, splitting, and coalescence with each other or other bubbles (e.g., bubble clusters from the CZ) to form a micro-bubble cloud.<sup>22</sup> These micro-bubbles exhibited chaotic motion with continuous splitting and coalescence during oscillation, which perpetually eroded the surface of the MWCNT clusters by impelling liquid entrainment through micro water jets<sup>22,33</sup> (known as the sono-capillary effect) or loosening the clusters from the inside. This corresponded to the 'comet' feature observed in Fig. 9a–c in the top ROI and Fig. 10 in the bottom ROI where the combination of micro-bubble clusters and agglomerate acted as a 'comet nucleus,' and the detached debris acted as a 'comet tail.' After a period of oscillation, these micro-bubbles would either separate from the parent agglomerates through implosion [induced by CZ, such as in Fig. 9a or after coalescence with a nearby bubble, as in Fig. 9b or continue loosening (Figs. 9c and 10) before finally being sheared by the central streaming flow (Figs. 9c and 10i).

### **SUMMARY OF DEAGGLOMERATION MECHANISMS**

The observed deagglomeration mechanisms of MWCNTs during UST (the stabilized CZ stage) are given schematically in Fig. 11. In summary, during the UST of MWCNT-water nanofluid, the deagglomeration events occurred both inside and outside the CZ. However, most particles did not show a significant change in size or shape after entering the CZ, which may be due to the lack of UST time or limitations of the high-speed camera. We suspect that the shockwaves generated by the bubble cloud<sup>22,34</sup> could also create some surface defects or expand the agglomerates due to extremely high local pressure, assisting deagglomeration at a later stage. However, this hypothesis needs to be further investigated by elongating the UST time

and using a more advanced lens and camera. The micro-bubbles, on the other hand, created clear particle breaking or loosening events from the surface or inside the agglomerates during their oscillation motion. This observation can be explained by the sono-capillary effect, where a liquid micro-jet was generated and penetrated the bulk agglomerates during oscillations of micro-bubbles. After a period of oscillation, these micro-bubbles could either implode (under the activation of CZ or after coalescence with other bubbles) or shear by the jet flow, which further dispersed the MWCNTs.

### **CONCLUSION**

In this paper, UST assisted deagglomeration and dispersion of MWCNTs in DI water by UST were captured and analyzed for the first time by using high-speed imaging and numerical modeling. For images captured at wider FoV, PIV analysis was applied to calculate average flow speeds at three different amplitudes. Then, the results were compared with numerical modeling which suggested the PIV failed to capture the acoustic streaming jet flow directly underneath the sonotrode due to its 2D nature and limited spatial resolution. However, the remainder of the flow field matched well with the simulation results, providing model validation.

Images taken at 10,000 fps showed that deagglomeration can be observed in both ROIs before and after a stabilized CZ was formed. For the top ROI, deagglomeration was observed immediately after the emerging of a CZ. However, after the CZ was stabilized, most agglomerates showed no significant changes after passing through the bubble cloud, probably due to limited camera resolution and short UST time. The observed deagglomeration events in the CZ showed particle peeling and rupture manifestations which were tentatively attributed to shockwaves generated by the imploding bubble cloud. For the bottom ROI, all the observed deagglomeration events showed agglomerate loosening or surface particles breaking off at the initial stage. These effects were mainly attributed to the oscillation and coalescence of the surface bubbles or air pockets inside the agglomerate. After a period of time, these bubbles either imploded (under the activation of CZ or after coalescence with other bubbles) or were sheared by the jet flow which further dispersed the MWCNTs.

Moreover, the general findings in this paper may apply to a wide range of CNTs, including single-walled, double-walled, and larger carbon nanofibers, with a range of graphitic plane orientations, as well as other carbon nanomaterials as classified elsewhere.<sup>35</sup> The dispersal of these materials could be studied in water, particularly with the addition of established surfactants and amphiphiles, or

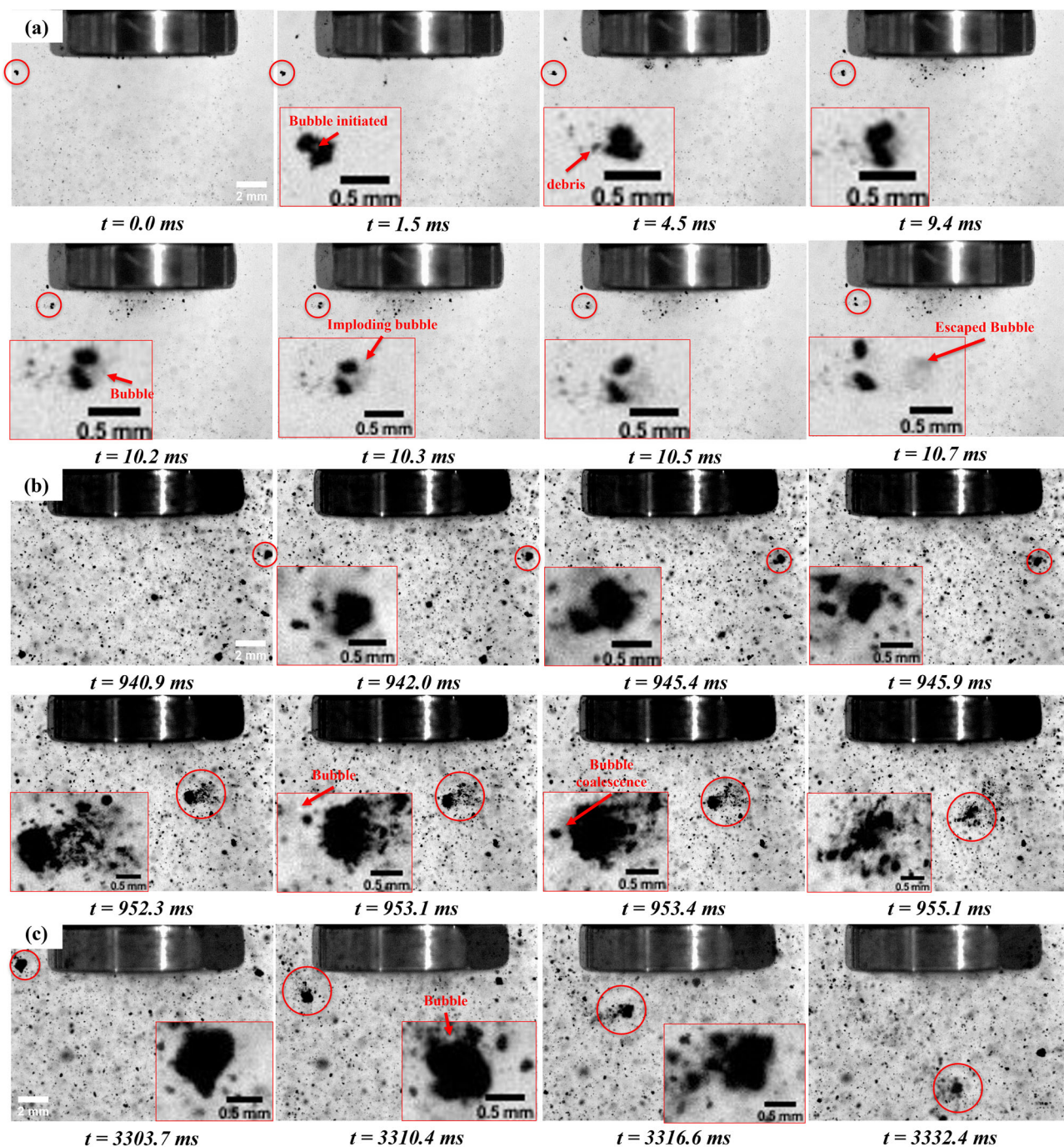


Fig. 9. Snapshots of agglomerates interacting indirectly with the CZ at the stabilized CZ stage. (a) Particle rupture due to the implosion of an oscillating micro-bubble inside the agglomerate. The implosion was believed to be activated by the CZ (20% amplitude) (See supplementary video 7). (b) Particle breaking due to the violent implosion of the oscillation micro-bubble inside the agglomerate. The implosion was activated after coalescence with another bubble (20% amplitude) (See supplementary video 8). (c) Particles loosening during bubble oscillation and subsequently shear by the streaming flow (20% amplitude) (See supplementary video 9). The elapsed time after the sonotrode was switched on is given at the bottom of each picture.

other solvents. With further quantification of the thresholds for different mechanisms, the simulations will allow the required UST conditions to be tailored to particular nanofluid and specific dispersion vessels/sonotrode geometries. The methods may be readily applied to other entangled

agglomerates of high aspect ratio nanoparticles, including synthetic materials such as dichalcogenide nanotubes [e.g.,  $(\text{Mo,W})(\text{S,Se})_2$ ], semiconductor nanowires,<sup>36</sup> and natural products such as bacterial cellulose.<sup>37</sup>

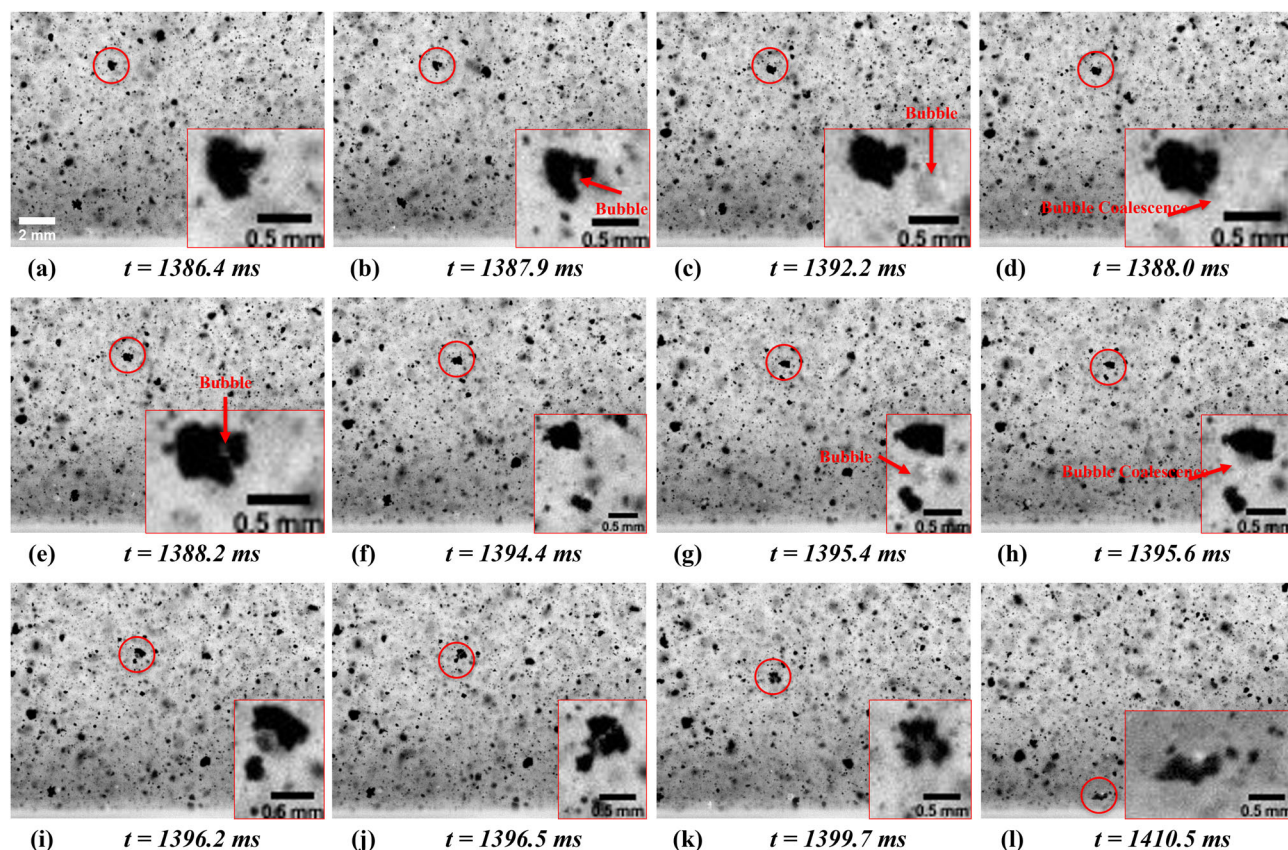


Fig. 10. Particles loosening during bubble oscillation and subsequently sheared by the streaming flow in the bottom ROI (40% amplitude) (See supplementary video 10). The elapsed time after the sonotrode was switched on is given at the bottom of each picture.

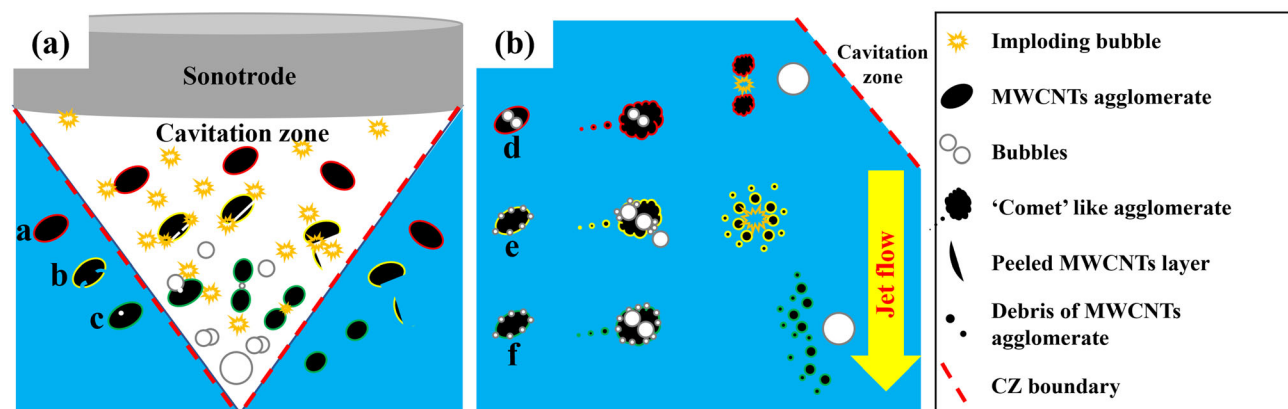


Fig. 11. A summary of the breaking mechanism inside the CZ (a) and outside the CZ (b) in the stabilized CZ stage. Within the sketch, event *a* corresponds to Fig. 8(a–b) (no change observed), *b* corresponds to Fig. 8(c) (peeling-off event); *c* corresponds to Fig. 8(d) (particle rupture); *d* corresponds to Fig. 9(a), *e* corresponds to Fig. 9(b), and *f* corresponds to Figs. 9(c) and 10: *d–f* all representing the “comet” feature with the particles moving from left to right.

## ACKNOWLEDGEMENT

We would like to thank Mr Franco Giammaria and Dr Isabella Fumarola for helping us to set up the imaging system for the experiments at Imperial College, London. The helpful suggestions about data acquisition and processing from Mr Taihang Zhu at Imperial College were also gratefully acknowledged.

## CONFLICT OF INTEREST

On behalf of all authors, the corresponding author states that there is no conflict of interest.

## OPEN ACCESS

This article is licensed under a Creative Commons Attribution 4.0 International License, which permits use, sharing, adaptation, distribution and

reproduction in any medium or format, as long as you give appropriate credit to the original author(s) and the source, provide a link to the Creative Commons licence, and indicate if changes were made. The images or other third party material in this article are included in the article's Creative Commons licence, unless indicated otherwise in a credit line to the material. If material is not included in the article's Creative Commons licence and your intended use is not permitted by statutory regulation or exceeds the permitted use, you will need to obtain permission directly from the copyright holder. To view a copy of this licence, visit <http://creativecommons.org/licenses/by/4.0/>.

## SUPPLEMENTARY INFORMATION

The online version contains supplementary material available at <https://doi.org/10.1007/s11837-022-05274-4>.

## REFERENCES

- D. Son, J. Lee, D.J. Lee, R. Ghaffari, S. Yun, S.J. Kim, J.E. Lee, H.R. Cho, S. Yoon, S. Yang, S. Lee, S. Qiao, D. Ling, S. Shin, J.-K. Song, J. Kim, T. Kim, H. Lee, J. Kim, M. Soh, N. Lee, C.S. Hwang, S. Nam, N. Lu, T. Hyeon, S.H. Choi, and D.-H. Kim, *ACS Nano* 9, 5937. <https://doi.org/10.1021/acsnano.5b00651> (2015).
- N. Behabtu, M. Green, and M. Pasquali, *Nano Today* 3, 24. [https://doi.org/10.1016/s1748-0132\(08\)70062-8](https://doi.org/10.1016/s1748-0132(08)70062-8) (2008).
- Z. Baig, O. Mamat, and M. Mustapha, *Crit. Rev. Solid State Mater. Sci.* 43, 1. <https://doi.org/10.1080/10408436.2016.1243089> (2018).
- H. Dieringa, *Metals* 8, 431. <https://doi.org/10.3390/met8060431> (2018).
- G.I. Eskin, *Ultrasonic treatment of light alloy melts* (Gordon and Breach Science Publishers, Amsterdam, The Netherlands, 1998).
- D. Tan, T.L. Lee, J.C. Khong, T. Connolley, K. Fezzaa, and J. Mi, *Metall. Mater. Trans. A* 46, 2851. <https://doi.org/10.1007/s11661-015-2872-x> (2015).
- B. Wang, D. Tan, T.L. Lee, J.C. Khong, F. Wang, D. Eskin, T. Connolley, K. Fezzaa, and J. Mi, *Acta Mater.* 144, 505. <https://doi.org/10.1016/j.actamat.2017.10.067> (2018).
- L. Ma, F. Chen, and G. Shu, *J. Mater. Sci. Lett.* 14, 649. <https://doi.org/10.1007/bf00586167> (1995).
- Y.Y. Huang, and E.M. Terentjev, *Polymers* 4, 275. <https://doi.org/10.3390/polym4010275> (2012).
- T. Nowak, C. Cairós, E. Batyrshin, and R. Mettin, Acoustic streaming and bubble translation at a cavitating ultrasonic horn. *AIP Conf. Proc.* 1685, 020002. <https://doi.org/10.1063/1.4934382> (2015).
- I. Tzanakis, W.W. Xu, D.G. Eskin, P.D. Lee, and N. Kotsovinos, *Ultrason. Sonochem.* 27, 72. <https://doi.org/10.1016/j.ultsonch.2015.04.029> (2015).
- L. Vaisman, G. Marom, and H.D. Wagner, *Adv. Func. Mater.* 16, 357. <https://doi.org/10.1002/adfm.200500142> (2006).
- Y.Y. Huang, T.P.J. Knowles, and E.M. Terentjev, *Adv. Mater.* 21, 3945. <https://doi.org/10.1002/adma.200900498> (2009).
- G. Pagani, M.J. Green, P. Poulin, and M. Pasquali, *Proc. Natl. Acad. Sci.* 109, 11599. <https://doi.org/10.1073/pnas.1200013109> (2012).
- A. Lucas, C. Zakri, M. Maugey, M. Pasquali, P. Van Der Schoot, and P. Poulin, *J. Phys. Chem. C* 113, 20599. <https://doi.org/10.1021/jp906296y> (2009).
- J. Hilding, E.A. Grulke, Z.G. Zhang, and F. Lockwood, *J. Dispers. Sci. Technol.* 24, 1. <https://doi.org/10.1081/dis-120017941> (2003).
- M.-C. Yang, M.-Y. Li, S. Luo, and R. Liang, *Int. J. Adv. Manuf. Technol.* 82, 361. <https://doi.org/10.1007/s00170-015-7348-z> (2016).
- Q. Zaib, I.A. Khan, Y. Yoon, J.R.V. Flora, Y.-G. Park, and N.B. Saleh, *J. Nanosci. Nanotechnol.* 12, 3909. <https://doi.org/10.1166/jnn.2012.6212> (2012).
- Q. Zaib, and F. Ahmad, *ACS Omega* 4, 849. <https://doi.org/10.1021/acsomega.8b02965> (2019).
- J.A. Morton, M. Khavari, L. Qin, B.M. Maciejewska, A.V. Tyurnina, N. Grobert, D.G. Eskin, J. Mi, K. Porfyrakis, P. Prentice, and I. Tzanakis, *Mater. Today* 49, 10. <https://doi.org/10.1016/j.mattod.2021.05.005> (2021).
- D.G. Eskin, I. Tzanakis, F. Wang, G.S.B. Lebon, T. Subroto, K. Pericleous, and J. Mi, *Ultrason. Sonochem.* 52, 455. <https://doi.org/10.1016/j.ultsonch.2018.12.028> (2019).
- A. Priyadarshi, M. Khavari, T. Subroto, P. Prentice, K. Pericleous, D. Eskin, J. Durodola, and I. Tzanakis, *Ultrason. Sonochem.* 79, 105792. <https://doi.org/10.1016/j.ultsonch.2021.105792> (2021).
- G.S.B. Lebon, I. Tzanakis, K. Pericleous, D. Eskin, and P.S. Grant, *Ultrason. Sonochem.* 55, 243. <https://doi.org/10.1016/j.ultsonch.2019.01.021> (2019).
- C. Beckwith, G. Djambazov, K. Pericleous, T. Subroto, D.G. Eskin, D. Roberts, I. Skalicky, and I. Tzanakis, *Metals* 11, 674. <https://doi.org/10.3390/met11050674> (2021).
- G.S.B. Lebon, G. Salloum-Abou-Jaoude, D. Eskin, I. Tzanakis, K. Pericleous, and P. Jarry, *Ultrason. Sonochem.* 54, 171. <https://doi.org/10.1016/j.ultsonch.2019.02.002> (2019).
- L. Zhang, X. Li, R. Li, R. Jiang, and L. Zhang, *Mater. Sci. Eng. A* 763, 138154. <https://doi.org/10.1016/j.msea.2019.138154> (2019).
- F.J. Trujillo, *Ultrason. Sonochem.* 47, 75. <https://doi.org/10.1016/j.ultsonch.2018.04.014> (2018).
- J.B. Keller, and M. Miksis, *J. Acous. Soc. Am.* 68, 628. <https://doi.org/10.1121/1.384720> (1980).
- M.C. Schenker, M.J.B.M. Pourquié, D.G. Eskin, and B.J. Boersma, *Ultrason. Sonochem.* 20, 502. <https://doi.org/10.1016/j.ultsonch.2012.04.014> (2013).
- I. Tzanakis, G.S.B. Lebon, D.G. Eskin, and K.A. Pericleous, *Ultrason. Sonochem.* 34, 651. <https://doi.org/10.1016/j.ultsonch.2016.06.034> (2017).
- M. Khavari, A. Priyadarshi, A. Hurrell, K. Pericleous, D. Eskin, and I. Tzanakis, *J. Fluid Mech.* 915, 3. <https://doi.org/10.1017/jfm.2021.186> (2021).
- H. Liu, J. Zhai, and L. Jiang, *Soft Matter* 2, 811. <https://doi.org/10.1039/B606654B> (2006).
- C.D. Ohl, and R. Ikink, *Phys. Rev. Lett.* 90, 21. <https://doi.org/10.1103/physrevlett.90.214502> (2003).
- A. Priyadarshi, M. Khavari, S.B. Shahrani, T. Subroto, L.A. Yusuf, M. Conte, P. Prentice, K. Pericleous, D. Eskin, and I. Tzanakis, *Ultrason. Sonochem.* 80, 105820. <https://doi.org/10.1016/j.ultsonch.2021.105820> (2021).
- I. Suarez-Martinez, N. Grobert, and C.P. Ewels, *Carbon* 50, 741. <https://doi.org/10.1016/j.carbon.2011.11.002> (2012).
- Y. Huang, X. Duan, Y. Cui, and C.M. Lieber, *Nano Lett.* 2, 101. <https://doi.org/10.1021/nl015667d> (2002).
- G.F. Picheth, C.L. Pirich, M.R. Sierakowski, M.A. Woehl, C.N. Sakakibara, C.F. De Souza, A.A. Martin, R. Da Silva, and R.A. De Freitas, *Int. J. Biol. Macromol.* 104, 97. <https://doi.org/10.1016/j.ijbiomac.2017.05.171> (2017).

**Publisher's Note** Springer Nature remains neutral with regard to jurisdictional claims in published maps and institutional affiliations.